Final Technical Report

Development and Validation of a Simulation Tool to Predict the Combined Structural, Electrical, Electrochemical and Thermal Responses of Automotive Batteries

Award Number: DE-EE0007288
Prime Recipient: Ford Motor Company
Partners: Oak Ridge National Laboratory

1. **Prime Recipient:** Ford Motor Company (Ford)
   Award Number: DE-EE0007288
   Award Type: Cooperative Agreement
   Partners: Oak Ridge National Laboratory (ORNL)
   Principal Investigators:
   Ford: Dr. Chulheung Bae (cbae@ford.com)
   ORNL: Dr. Srdjan Simunovic (simunovics@ornl.gov)
   Ford Contracts Manager: Melissa Hendra

   Federal Agency: DOE/NETL EERE
   Technology Manager: Brian Cunningham
   Program Manager: Adrienne Riggi

2. **Project Title**: Development and Validation of a Simulation Tool to Predict the Combined Structural, Electrical, Electrochemical and Thermal Responses of Automotive Batteries

3. **Grant Period:** January 1, 2016 – March 31, 2020
   Date of Report: March 31, 2020

   FOA: DE-FOA-0001201
   DUNS Number: 049967672

4. **Project Objectives:**
   The objective of this project was to develop and validate a simulation tool with unprecedented fidelity to predict the combined structural, electrical, electrochemical and thermal (SEET) response of automotive batteries to crash-induced crush and short circuit. The project included development of a practical simulation tool to predict the combined structural, electrical, electrochemical, and thermal responses of automotive batteries to crash induced crush and short circuit, and validate it for conditions relevant to automotive crash. In addition, the project also:

   Developed material constitutive models and finite element method (FEM) element formulations that capture the mechanical response of cell components, including the case material, electrodes and separator.

   Clearly identified the required input parameters for the material constitutive models, FEM element formulations, and exothermic, electrochemical reaction state equations governing multi-physics phenomena during crush-induced electrical short, thermal ramp, and overcharge conditions.

   Designed and executed a test matrix encompassing automotive crash strain rates at a number of kinetic energy levels and physical orientations likely to occur in vehicle impacts.

   Developed integrated modeling tools that demonstrate high-fidelity predictions of the onset of thermal runaway from the experimental test matrix using commercially available cells, module, and packs, spanning multiple chemistries relevant to automotive applications.

Maintained high-fidelity predictions while exploring methods to reduce the computational complexity of the model, and deliver a practical tool that is integrated with the laboratory's Open Architecture Software (OAS), for a broad customer base within automotive product development.

5. Background:

Battery safety is one of the most important design factors of electrified vehicles (EVs) since battery failure may lead to a catastrophic consequence. To improve the safety of battery systems in EVs, battery behaviors under various abuse conditions should be well understood. One way to examine battery response under extreme conditions is to conduct abuse tests in different scenarios. They can provide first-hand pass/fail information on battery safety, but they are usually expensive and time-consuming, which is inconvenient during design iterations and optimization. On the other hand, computational modeling can predict the battery behaviors in a more efficient and cost-effective way, which becomes an important tool to evaluate battery safety. Modeling battery responses and failure is challenging since it involves multiple coupled physical processes, needs to consider complex material properties and is computationally intensive. This project aims to develop a practical simulation tool to predict the combined structural, electrical, electrochemical, and thermal responses of automotive batteries to crash-induced crush and short circuit and validate it for conditions relevant to automotive crash. Advanced material constitutive models will be utilized to capture the mechanical response of cell components. Moreover, methods will be developed to reduce computational complexity of the model and allow battery safety simulations to extend from cell-level to module/pack level with affordable computational resources.

6. Milestone Review:

The original three-year project was extended fifteen months, primarily due to difficulties encountered by the original external testing laboratory. With the extension, all milestones were completed, as shown in Table 1.

7. Results and Discussion:

Task 0.0 – Overall Project Management and Planning and Coordination: *The objectives for the project management portion of the work are to provide project planning, coordination, and reporting as required to successfully achieve the overall objectives of the project.*

Subtask 0.1 – Project Management and Planning

- Quarterly reviews were held with DOE and TARDEC every quarter.
- All quarterly reports were submitted on time.
- The original end date was extended from December 31, 2018 to March 31, 2020.
- The overall project constituents and progress of Alpha and Beta versions are summarized in Figure 1.
- As shown in Table 1, all tasks were completed successfully.

Table 1. Complete list of milestones and decision points for the project.

Budget Period	Task	Description	Type	Start Date	End Date	% Completed
BP1	1.2	Hardware selected	M1	1/1/2016	3/31/2016	100%
	1.1	Analysis of existing models completed	M2	1/1/2016	6/30/2016	100%
	1.1	Assumptions formulated	M3	1/1/2016	6/30/2016	100%
	1.6.3	Test site selected	M4	7/1/2016	9/30/2016	100%
	1.5	Preliminary version of software demonstrated	DP1		12/31/2016	completed
BP2	1.4/2.2	Cell characterization experiments complete	M5	4/1/2016	6/30/2017	100%
	1.3/2.1	Multi-physics solvers complete	M6	4/1/2016	3/31/2017	100%
	1.5/2.3	Model integration complete	M7	10/1/2016	6/30/2017	100%
	2.5	Beta model development assumptions	M8	7/1/2017	9/30/2017	100%
	2.4/1.6	Validation of Alpha version model	DP2		3/30/19	100%
BP3	2.6/3.1	Select & build hardware complete	M9	7/1/2017	3/31/2018	100%
	2.7/3.2	Multi-physics solvers and material models	M10	1/1/2018	8/31/19	100%
	3.3/3.4	Beta version model input and integration	M11	1/1/2018	8/31/19	100%
	3.5	Validation of Beta version model	M12	10/1/2018	11/30/19	100%

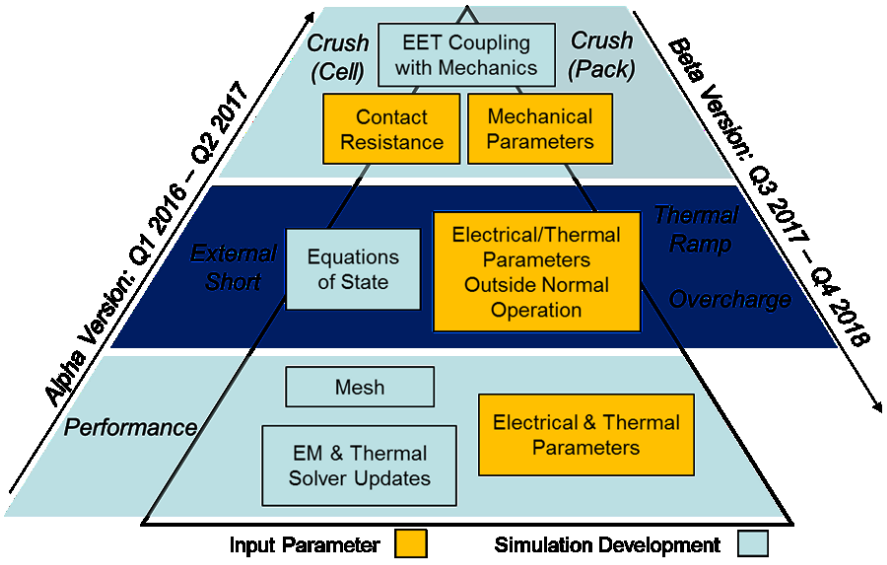

Figure 1. Project schematic showing major constituents and progression of Alpha and Beta versions.

Task 1 - Develop and validate Alpha version battery modeling tool:
This task will result in delivery of a prototype simulation tool capable of predicting the combined structural, electrical, electrochemical, and thermal response of an automotive battery cell subjected to abuse conditions.

Multi-physics battery safety model development:

The multi-physics model developed here aims to capture the mechanical, electrical, electrochemical and thermal responses of batteries simultaneously. When a cell deforms, its displacement field is obtained from the momentum balance equation

$$\nabla \cdot \sigma + \rho \boldsymbol{b} = \rho \boldsymbol{a} \qquad [1]$$

where σ is the Cauchy stress tensor, ρ is the density, $\boldsymbol{b}$ is the body force per unit mass and $\boldsymbol{a}$ is the acceleration. The temperature distribution in a cell is given by the energy balance equation

$$\rho c_p \frac{\partial T}{\partial t} = \nabla \cdot (k \nabla T) + \dot{q} \qquad [2]$$

where c_p is the heat capacity, T is temperature, t is time, k is the thermal conductivity, and $\dot{q}$ is the heat source term that contains irreversible heat generation associated with ohmic and kinetic loss across the unit cell, reversible heat generation due to entropy and Joule heating induced by in-plane current within the current collectors. In the case of short-circuit, the heat source term includes Joule heating due to short-circuit current between current collectors. The electrical potential distribution in a cell is obtained by solving the charge balance equation

$$\nabla \cdot (\kappa \nabla \varphi) = i/L \qquad [3]$$

where κ is the electric conductivity, φ is the electrical potential, L is the thickness of current collector, and i is the transverse current density given by the battery model. The electrochemical behaviors of a cell are represented by the Randles circuit model (an equivalent circuit model) because of its reasonable accuracy and computational efficiency that is required by large-scale simulations. A Randles circuit consists of an open-circuit voltage, an internal resistance, and a resistance-capacitance (RC) pair for polarization and damping effects. The transverse current density i across each Randles circuit is given by

$$\Delta\varphi = u - ir_0 - v_D \quad [4]$$

$$\frac{dv_D}{dt} = \frac{i}{c_D} - \frac{v_D}{r_D c_D} \quad [5]$$

where $\Delta\varphi$ is the potential drop in a Randles circuit, u is the open-circuit voltage, r_0 is the internal resistance, v_D is the diffusion overpotential, r_D and c_D are the resistance and capacitance of the RC pair, respectively. When a cell is shorted, the Randles circuits in the shorted area are replaced by short-circuit resistances.

The above model has been implemented in the commercial software LS-DYNA, where Eqs. (1), (2) and (3-5) are solved by the mechanical, thermal and electromagnetic (EM) solvers, respectively. The coupling between these solvers can be briefly described as follows. The mechanical solver provides geometry/deformation of a cell to other solvers, and its solution is affected by temperature via temperature-dependent structural properties. The EM and thermal solvers are connected such that the (transverse and in-plane) current densities contribute to the heat source terms $\dot{q}$ and therefore affect temperature, and at the same time, temperature affects current densities and electric potentials since transport and material properties (such as r_0, r_D, c_D) depend on temperature. In the EM solver, the transverse current densities i obtained from the Randles circuit model determine the current source terms in the charge balance equation, and the latter provides the electrical potential φ at current collectors that affects the current passing through the circuit.

Numerical implantation of the battery safety model:

To develop methods to reduce computational complexity, the model has been implemented in LS-DYNA in three formats: solid model, tshell model and macro model. In the solid model, each individual component is resolved and represented by one layer of solid elements (see Fig. 2a). Each component may have different thickness and material properties. A network of Randles circuits connect pairs of nodes in consecutive opposite current collectors (see Fig. 2d). In the tshell model, composite tshell elements with larger thickness are used instead of solid elements (see Fig. 2b). Along the thickness direction, a composite tshell element contains multiple integration points, and each of them corresponds to one individual component. The time saving in the tshell model comes from the mechanical solver that applies the equivalent single layer theory to solve for nodal displacements. The EM and thermal solvers, on the other hand, rebuild an internal mesh that resolves each individual component and then solve equations on it. The macro model treats a cell as a homogeneous solid, where large solid elements can be used (see Fig. 2c). Different from previous homogenized models, the macro model considers the thermal, electrical and electrochemical responses of batteries. The latter is realized by assuming that each node contains two electrical potentials connected by one Randles circuit (see Fig. 2e). These two potentials act like electrical potentials in positive and negative current collectors. They are solved separately with electrical conductivities adjusted to account for the difference between the thickness of the cell and current collectors.

To evaluate the performance of these three models, we examine the coupled responses of a 21Ah lithium-ion pouch cell during and after impacts. The cell size is 165mm × 220mm × 5.33mm, and the thickness of individual positive and negative current collectors, positive and negative electrodes and separator is 15μm, 9μm, 53μm, 64μm and 23μm, respectively. The schematic description of three models is shown in Fig. 3. In simulations, the pouch cell is placed on a fixed rigid flat platen, and the indenter (either a semi-sphere with 75mm radius or a semi-cylinder with 50mm radius) moves toward the cell at a constant speed of 2m/s. Two types of simulations are conducted. The first one only involves the mechanical solver, where the indenter moves until the cell deforms 85% in its thickness direction. The second one is the multi-physics simulation that activates the coupled mechanical, EM and thermal solvers. Here the indenter moves 0.5ms (for the semi-sphere indenter) or 0.6ms (for the semi-cylinder indenter). After that, all parts become rigid, while thermal, electrical and electrochemical responses of the cell keep updated until the end of simulations. In the solid and tshell models, a short-circuit occurs when the distance between two consecutive opposite current collectors is reduced by 10% of its original value. A short-circuit occurs in the macro model when the effective strain reaches 4.5%.

Fig. 4a shows the force-displacement relationship of the cell in different models, where only the mechanical solver is activated. It can be seen that the loading force of the semi-cylindrical indenter increases faster than the semi-sphere indenter, which is due to the larger contact area and therefore resistance to penetration in the former. Figs. 4b-4c show the evolution of cell voltage and average state of charge (SOC) from the multi-physics simulations. It can be seen that for both indenters, the cell becomes shorted during the impact period (0.5/0.6ms), while the voltage and SOC drop rapidly. Since the SOC in shorted circuits is set to zero, the average SOC drops suddenly when multiple circuits are shorted simultaneously. The voltage and SOC drop to lower values with the semi-cylindrical indenter because the shorted area in that case is larger. After the impact, the voltage and SOC decrease gradually. High current in the shorted area causes local temperature increase (see Figs. 4d-4i), which may lead to thermal runaway eventually.

Fig. 4 demonstrates that all three models can capture general responses of a cell during and after impact and give comparable results in relevant quantities such as loading force, voltage and temperature. The detailed behaviors of individual components, however, can be obtained only from solid or tshell models since the macro model utilizes homogenized properties. The relative computational time of different models in each impact event is shown in Fig. 5. It shows that the tshell model is more than ten times faster than the solid model. Due to the internal mesh built by the thermal and EM solvers in the tshell model, the time spent by these two solvers are similar in solid and tshell models. Thus, the time saving of the tshell models comes from the usage of the equivalent single layer theory in the mechanical solver. The macro model, on the other hand, is faster than the solid model by more than two orders of magnitude since it requires fewer elements and can utilize larger time steps due to the larger characterization length of the elements.

Figs. 4 and 5 show that to conduct multi-physics battery simulations at large-scale (i.e., module/pack level), the macro model is preferred when homogenized properties (such as loading force, voltage and temperature) are of interest. It is computationally efficient and can be reasonably accurate after calibration. On the other hand, when the component-level behaviors (such as failure of a specific separator) are relevant, solid or tshell models should be used since they contain information of each individual layer. Solid models are generally only suitable for cell-level simulations because of its computational intensity, while tshell models can be used in

module/pack level simulations. In LS-DYNA, these three types of models can be switched without difficulties. As such, after calibrating material models, the battery safety simulation can be extended from cell-level to module/pack-level without losing much accuracy using reasonable computational resources.

Material models development:

Active materials occupy the largest volume fraction in automotive battery cells. That is a result of the desire to store the maximum amount of energy in the cell in order to increase its energy efficiency. Consequently, the mechanical response of the cell jellyroll is dominated by the mechanical response of active materials. Their microstructure is an assembly of electrochemically active particles, held together by bonding agent and the deformation imparted by the calendaring process. In addition to their volumetric prevalence, the active materials have little or no elastic response and very low strength compared to the other jellyroll components, so that the deformation preferentially partitions into them. Our previous experiments confirmed the initial premise of suitability of soil mechanics models for modeling deformation of active materials. Given that LS-DYNA is the dedicated solver for the research project, we have investigated utility of the existing models in LS-DYNA for modeling active materials. Numerous soil and concrete material models that may be relevant to our purpose exist in the code. Given the lack of standardized mechanical testing for active materials and their availability for testing in a sufficient volume, we focused to the models with limited number of experimentally measurable parameters and ability to model characteristic behavior observed in experiments.

Cap models are currently the most used type of constitutive models for modeling of soils in computational simulations. They are based on the theory of plasticity and contain familiar concepts of elastic domain, yield surfaces, and hardening, failure limits. More complex variations include concepts of softening and residual strength. The form of yield surfaces may differ between the models, but they all have some type of pressure-dependent movable cap for describing hardening behavior. This cap was originally added enhance ideally plastic models to account for the irreversible compaction under pressure. Two relevant cap models for our purpose in LS-DYNA were MAT_025 (*MAT_GEOLOGIC_CAP_MODEL) and MAT_145 (*MAT_SCHWER_MURRAY_CAP_MODEL).

MAT_025 is quasi-static material model that does not have extensions for modeling material softening, damage and strain rate sensitivity. The model consists of a failure (perfect plasticity) surface, and the elliptic cap (hardening) surface. A simplified version of the model is illustrated in Fig. 6. The J1 and J2 denote the negative of the first stress invariant and the second invariant of the deviatoric stress tensor, respectively. The role of the failure surface, Fe, is to limit the amount of shear that the material can support without failure. If the stress is within yield surfaces, the response is elastic. If the stress reaches a yield surface, the material deforms plastically in the direction of the normal to the surface. The density increases (compaction) and material hardens when stress is on the cap surface, Fc. The density decreases (dilatation) when the stress state reaches the failure line. Dilatation implies softening and strain localization. This model has discontinuity at the intersection of two yield surfaces, so that the transition from the compaction to dilatation under shear localization is not continuous and requires special handling.

Standardized testing for soil materials require large volumes of material and a large number of experiments to traverse yield surfaces and hardening parameters. In our work, the material parameters for MAT_025 were derived from the limited experiments for active materials

reported in the literature, tests conducted in-house, and engineering estimates for feasible ranges of values. In particular, parameters for MAT_025 were derived by conversion of Drucker-Prager cap model from the literature. Simulations of experiments were conducted, and reasonably close match was found.

Material model MAT_025 does not have damage or strain-rate sensitivity sub-models. That limits its capability for modeling progressive failure, residual strength, and the effect of impact speed. In our impact experiments, cells undergo considerable damage, so that these model features were of interest and we explored feasibility of modeling active materials in cells under impact with material model MAT_145. Material model MAT_145 is an extension of MAT_025 in that it: (a) uses three stress invariants compared to two in MAT_025, (b) implements continuous transition from compaction to dilatant deformation, (c) adds damage and softening models, and (d) includes the effect strain rate dependency. Naturally, model capability increase tradeoff involves commensurate increase in number of model parameters. The continuous yield surface also leads to better stability in computational simulations. Due to the continuity implementation model of the yield surfaces, for the same basic parameters, MAT_145 is inherently stronger than MAT_025, but given the significant uncertainties in the properties, we did not make modifications to adjust the model parameters.

All model parameters developed for MAT_025 were used in MAT_145, as well. Multiaxial test experiments for exploring triaxial stress response were not conducted, so that model effectively utilizes two stress invariants, only. The damage and softening models in MAT_145 describe the deterioration of material strength and stiffness once limit stress surface for certain stress type is reached. The strength limit surfaces ultimately collapse to the residual stress surfaces for fully failed material. The damage in MAT_145 can occur in three modes; tensile (brittle), shear (dilatation), and ductile (compression). Tensile damage includes tensile failure stress, and two parameters describing the fraction of the tensile failure stress when the onset of strength deterioration initiates, and the rate of the stress softening, respectively. Similarly, for shear damage, two parameters exist to model the onset and deterioration of shear strength. As all our experiments we under compressive impact, we disregarded the damage in the tensile modes and investigated the sensitivity of parameters for modeling compressive (ductile) and shear damage. Two and three damage parameters are used for modeling compressive and shear failure mode, respectively, in MAT_145. For shear damage, parameter EFIT and FFIT determine the shape of the softening curve after damage start accumulating. Similarly, ductile damage parameters AFIT and BFIT, determine the shape of the softening curve when compressive damage starts accumulating. Ductile damage parameter RDAM0, determines strain energy threshold for damage. We treated the above dilatational and ductile damage parameters as empirical values for fitting to experiments due to lack of experimental procedures for relevant to active materials and battery cells. The range of values considered covers values that can be expected based on available experimental data. Values of AFIT and EFIT can be set to 1 for simplification. That leaves parameters BFIT, FFIT and RDAM0 for fitting. Viscoplasticity relaxation time parameter (VPTAU) is used to model the strain rate effect. In case when damage and strain rate effects are not considered, all these parameters have value 0.

We have varied the values of parameters BFIT, FFIT, RDAM0 and VPTAU, and compared the force-displacement curve of simulated the spherical impact on Type D cell, with experiments. We have selected the damage parameters and viscoplastic relaxation parameter based on the comparison, and the same damage parameters were used for anode and cathode materials.

Impact tests of pouch and prismatic cells:

To validate model predictions, impact testing was conducted with both pouch and prismatic cells along with different indenters and platens. Cell SOC was set to either 100% or 20% to see if the cell behaved differently during impact with differing amounts of stored energy. To conduct impact tests, a custom impact stand was designed and fabricated (see Fig. 7), where the impact energy can be adjustable through either impact velocity (directly proportional to the height at which the sled and indenter were dropped) or mass of the sled and indenter. The impact stand was designed to be able to provide any drop height from 0 m up to 1.8 m (measured from the top of the cell face to the bottom of the indenter). The mass of the impacting object can be varied by using lead weight bags placed inside the aluminum sled and the option of bolting steel plate weights to the top of the sled. Table 2 shows the conditions used for the cell impact testing.

During the impact testing the following signals were measured with a high-speed data acquisition system (100 kHz): cell voltage, cell surface temperature, impact force and indenter displacement (cell crush). In addition, a high-speed camera was used to record the impact event at 2,500 fps (see Fig. 8 for an image taken from the high-speed camera). Four HBM CFW-140 piezoelectric load cells and four CMA-2000 charge amplifiers were used to measure the force during the impact event. The specifications for the sensors can be found in Table 3 and Table 4. The load cells were mounted between the platen and the steel structure and located in the four corners of the platen. The charge amplifiers were located outside of the test cell near the DAQ system. The placement of the four load cells allowed for one to determine the orientation of the indenter with respect to the platen or if certain locations of the cell transmitted energy more easily than others. The sum of these loads gives the loading force experienced by a cell during impact. The displacement of the indenter during the impact event is measured using a Keyence LK-H152 laser displacement sensor, and its specifications is shown in Table 5. The laser displacement sensor was positioned such that the sensor was able to measure the indenter displacement 10-20 mm before the impact. In addition to data measurement, it was important for this testing that the indenter and platen be electrically non-conductive so that any short circuits that occurred were internal to the cell (e.g. the separator was cracked and allowed the anode and cathode to contact with one another). The indenters and platens were machined from aluminum so they could be anodized to be electrically non-conductive. A MIL-A-8625 Type III hard anodized coating was used to ensure that the coating would withstand repeated impact tests. Fig. 9 shows indenters and platens before and after anodization.

After the cell was impacted by the indenter, the indenter rebounded off the cell and traveled upwards in the air. However, gravity pulls the indenter back down, and without external influences the indenter will hit the cell again and eventually come to rest on top of the cell. To mimic a car crash, it was decided that the indenter had to impact the cell only once and then the indenter and sled had to be caught to keep it from impacting again. We used pneumatic cylinders that were installed underneath the platen & load cells and actuated them at the correct time to catch the sled and indenter. Significant effort was taken to characterize the response time of the pneumatic cylinders at different air pressures and with different rod extensions before actuation. Understanding the response time of the pneumatic cylinders allowed us to determine when to trigger the pneumatic system to stop the indenter from impacting the cell a second time. A number of preliminary tests were conducted to determine the height and mass required for causing cell failure (significant voltage drop or thermal runaway), and the selected

conditions are shown in Table 2. In these tests, if a cell was impacted without short-circuit or thermal runaway, it was sent to CT scan to examine the inside of the cell and attempt to identify any cracks within the jellyroll. Fig. 10 shows a sample of the results from CT scanning after a pouch cell was impacted by a semi-cylinder indenter. Note the crack through the thickness of the cell on the left-most image.

Table 2. Cell impact test matrix

Cell type	SOC	Platen type	Indenter shape	Drop weight (kg)	Drop height (m)
Pouch	100% & 20%	Flat, with trough*	R75mm semi-cylinder	75	0.5
		Flat	R75mm semi-sphere	70.2	0.5
Prismatic		Flat	R12.5mm semi-cylinder	91.7	1.75
		Flat	R75mm semi-sphere	94.5	1.7

* Trough is in the platen center, and four trough depths are tested: 41%, 100%, 170% and 200% of pouch cell thickness

Table 3. HBM CFW-140 piezoelectric load cell specifications

Load Cell Characteristic	Specification
Nominal (rated) Force	140 kN
Preload Required	14+ kN
Sensitivity	-4.3 pC/N
Max. Operating Force	168 kN
Breaking Force	280 kN
Fundamental Resonance Frequency	35 kHz

Table 4. HBM CMA-2000 charge simplifier specifications

Charge Amplifier Characteristic	Specification
Max. Charge Input	2000 nC
Time for Measuring Range Conversion	250 µs
Accuracy	±0.5%
Hysteresis, 0.5 x F_{nom}	< 0.05%
Linearity Error	< ±0.05%
Measurement Frequency Range	7 kHz (-3 dB) - 3.5 kHz (-1 dB)

Table 5. LK-H152 laser displacement sensor specifications.

Sensor Characteristic	Specification
Measurement Range	±40 mm (range varies with sample rate)
Sample Rate (9 steps selectable)	1 kHz – 392 kHz
Moving Average	1, 4, 16, 64, 256, 1024 samples
Linearity	±0.016 mm
Repeatability	0.25 μm
Sampling Delay (Sensor + Controller)	531.5 μs

Validation of the alpha-version model – Tshell model:

Quasi-static indentation of pouch cells:
The quasi-static indentation tests were performed with spherical and cylindrical indenters. The radius of the spherical indenter is 75mm, and the radius of the cylindrical indenter is 25mm. The pouch cell consists of 18 jellyroll layers along the thickness (z) direction. Each jellyroll layer is composed of one positive and negative current collector and two cathode anode and separator layers. Cathode and anode materials are modeled using MAT_145 without damage sub-models while current collectors and separators are modeled using LS-DYNA piecewise linear elastoplastic material model MAT_024. The pouch cover of thickness 0.1 mm at top and bottom of the cell is modeled using LS-DYNA elastic material (MAT_001). The comparison of the simulation results and experiments for quasi-static loading is shown in Fig. 11 for different loading cases.

Quasi-static shear of pouch cells:
The experiment setup and its simulation model for the shear of thin pouch (Type D) cell are shown in Fig. 12. The model uses a slice of the cell to simplify the simulation. Different cell slices and spans were considered to confirm the model assumptions. The experiment consists of two steps. During the first step, the cell is uniformly compressed in order to grip the cell surfaces and prevent cell from sliding during the shear loading stage. In the second step, the shear loading is applied. Correspondingly, the simulation also consists of 2 steps. In the first step of simulation, the cell is uniaxially compressed by 0.4 mm in the z direction. In the second step, the cell is deformed under shear loading as shown in Fig. 12(b). During the simulation, a total force on the support plates on one side of shear support was measured. This force contains both compression and shear responses. In order to obtain only the shear testing force component, we subtracted the pre-compression force in the first step of the simulation from the simulated total support force. The comparison of the measured and simulated shear force is shown in Fig. 13. The computational model does not account for extensive internal sliding and breakage observed in experiments, so that we consider results of the simulation is close to the experimental response.

Impact of pouch cells:
The impact tests were performed on pouch cells with cylindrical and spherical indenters, see Table 2. Comparison of simulations and experiments is shown in Fig. 14, where a pouch cell is placed on a flat platen. Damage sub-models are able to drop the simulated force magnitudes to the experimental levels. Extensive damage in the cells was noticed in the experiments. Elasto-

plastic materials of current collectors and separator do not have damage submodels. The impact tests were also conducted on pouch cells placed on the platens with grooved surface (see Table 2). Simulated force-displacement curves obtained for different groove depth configurations are shown in Fig. 15 and compared with experiments.

Impact of prismatic cells:
The impact tests were performed on prismatic cells with cylindrical and spherical indenters, see Table 2. Fig. 16 shows impact forces for different material model parameter combinations and comparison to experimental results. When using standard material damage parameters as selected in above examples (results marked “Damage”) the resulting force peak is close to the experiments and matches the duration of the force for the spherical impact. Since the jellyroll in prismatic cells is considerably thicker compared to pouch cells, this larger volume contains large volume of electrolyte which is expected to contribute to the strain rate sensitivity of the response. Impact force simulation results for standard damage model with added viscoplasticity parameter VPTAU=10, are marked in Fig. 16 as “Damage+VP”. Addition of viscoplasticity effect improves the accuracy in the early part of the force-displacement curve and may be relevant to modeling large stacks of cells.

Validation of the alpha-version model – Macro model:

Pouch (type D) and prismatic (type E) cell models have been developed and validated against experiments. The macro model is used to represent cells due to its computational efficiency, and the geologic cap model (MAT_025) is used to describe the mechanical behavior of the cell bulk since it can capture both shear and compaction failure. The failure conditions and the short-circuit conditions are selected to be the effective strain since the literature show that the failure condition of a large number of cells is strain based.

Fig. 17 shows the force – displacement relationships of a type D cell when it is impacted by either a sphere or a cylinder indenter. The platen is either flat (Fig. 17a) or with different depth of trough (Fig. 17b). The critical displacements when the cell fails as well as the peak force under all conditions (i.e., sphere/cylinder indenters, platens with/without trough) obtained by the model is within 10% of the experimental measurement. Moreover, it is found that the maximum loading force on a cell when the platen has trough is higher than the cell placed on a flat platen, while the peak loading force is not strongly dependent on the trough depth. In addition, it is shown that under the same impact conditions, the cell on the flat platen gets shorted, while the cells on platens with trough do not fail. All these observations are consistent with experimental results.

Fig. 18 shows the voltage – displacement relations of a pouch cell with different SOC levels on a flat platen impacted by different indenters. The mechanical failure conditions used in Fig. 17a are used as the short-circuit conditions. It is found that the critical displacement when the cell gets shorted (i.e., when the voltage starts to drop) obtained from the model is close to experiments. Fig. 19 shows the corresponding temperature evolution in above cases. It can be seen that for the 20% SOC cell, its temperature evolution obtained from model follows experimental data, while the temperature profile for the 100% SOC cell is significantly different in model and test due to thermal runaway. When the cell is 100% SOC, it has thermal runaway after the impact. The fire makes the measured temperature suddenly increase very fast. Since the fire process is not covered by the current model, the rapid temperature increase is not captured. The temperature growth before thermal runaway obtained from the model is similar to experiments as shown in Fig. 19b.

The models for the type E cell are also developed in the same fashion. Fig. 20 shows that the force – displacement relationships obtained from model is close to experiments under both indenters. With appropriate material parameters, the critical displacement and peak force is similar in model and experiments. Figs. 21-22 show the voltage – displacement relationships and temperature evolution of type E cells with different SOC levels and indenters. Similar to the pouch cells, the critical displacement when voltage drops is similar in model and experiments. The temperature evolution in the 20% SOC cell is similar in model and experiments, while large difference exists in the 100% SOC case that is probably due to thermal runaway.

Task 2 - Develop and validate Beta version battery modeling tool: Extend the developed Alpha version model to deliver a practical simulation tool for battery modules. Evaluate a variety of methods for reducing the structural model computational complexity. Demonstrate for abuse simulations of large-scale hardware.

Impact tests of pouch and prismatic modules:

The impact stand used for cell-level impact testing was updated for module-level testing (see Fig. 23). The upgraded setup included increasing the drop height, a new laser displacement sensor with longer range to accommodate the larger battery modules, a second winch to lift the indenter and sled beyond the reach of the flames after impact, steel platens and indenters, and an updated data acquisition system for recording five analog voltages, 16 thermocouple channels and new laser displacement sensor.

The new drop height was three meters (from the bottom of the indenter to the top of the module). This extended drop height allowed for a maximum estimated impact velocity of 5m/s. The 96-inch guide rods were replaced by 150-inch guide rods having similar diameter, mounting and linear bearings. The load cells used for cell-level testing were also used for module-level testing as the maximum force was still well within their safety limits. The indenters and platens were machined from carbon steel for the increased strength and harness required for the module-level impact testing. There parts were further treated with aluminum nitride, an extremely hard and non-conductive coating. This non-conductive coating would ensure that the indenter would not externally short circuit the module. The platens for the pouch-cell module and prismatic-cell module were designed to accommodate all three module orientations by bolting in spacers/adapters. The module test conditions can be found in Table 6, and the impact orientation can be found in Fig. 24.

Table 6. Module impact test matrix

Module type	SOC	Platen type	Indenter shape	Drop weight (kg)	Drop height (m)	Impact orientation
Pouch	100% & 20%*	Flat	R12.5mm semi-cylinder	92	3	X, Y, Z
			R75mm semi-sphere	95		X, Y, Z
Prismatic			R12.5mm semi-cylinder	114.7		X, Y, Z
			R75mm semi-sphere	117.2		X, Y, Z

* When SOC is 20%, the impact test was conducted along Z orientation only.

Validation of the beta-version model:

The impact tests for modules occur in three directions, so the module models where a module is impacted along three directions are developed. Since in all cell models, the cell is impacted along the through-thickness direction (i.e., Z direction), the module models where a module is impacted along the Z direction are calibrated and shown here. For other module models where impact occurs along X or Y directions, the qualitative features observed in experiments can be captured by the models, while improvements (such as using more accurate material data and/or failure condition for module components) are needed for quantitative comparison.

Fig. 25 shows the force – displacement and voltage - displacement relationships of a type D module when it is impacted by either a sphere or a cylinder indenter along the Z direction. It is found that the peak force and the displacement where the peak force occurs predicted by the models are close to experimental results. For the sphere indenter, the peak force corresponds to the failure of the top cell, which causes short-circuit (see Fig. 25b). For the cylinder indenter, there multiple force peaks that correspond to failure of different components. The first peak is due to the break of the module cover, and the subsequent peaks occur because the cells fail one by one. The short-circuit occurs when the top cell fails (around the second peak), which can be seen in Fig. 25c. Figs. 25b and 25c show that the critical displacement when the short-circuit occurs (i.e., when the voltage starts to drop) obtained from the model is close to experiments. Since there are four sub-modules in a module, we monitor the voltages in each of them in both models and tests. They both show that the first sub-module fails in the impact, which is expected since the first sub-module is the closest to the indenter and has the most severe damage due to impact.

Fig. 26 shows the force – displacement and voltage - displacement relationships of a type E module when it is impacted by either a sphere or a cylinder indenter along the Z direction. It is found that both simulations and tests show that the type E model exhibit similar responses when it is impacted by different indenters. Moreover, the peak force magnitude as well as the critical displacements predicted by the model match experiments well. In addition, from Figs. 26b and 26c we can see that in both cases, the short-circuit occurs before the force reaches its peak, and the displacements where the short-circuits occur observed in simulations are very close to experimental results. Both simulations and tests show that the cell 5 fails first since it is the closest to the indenter.

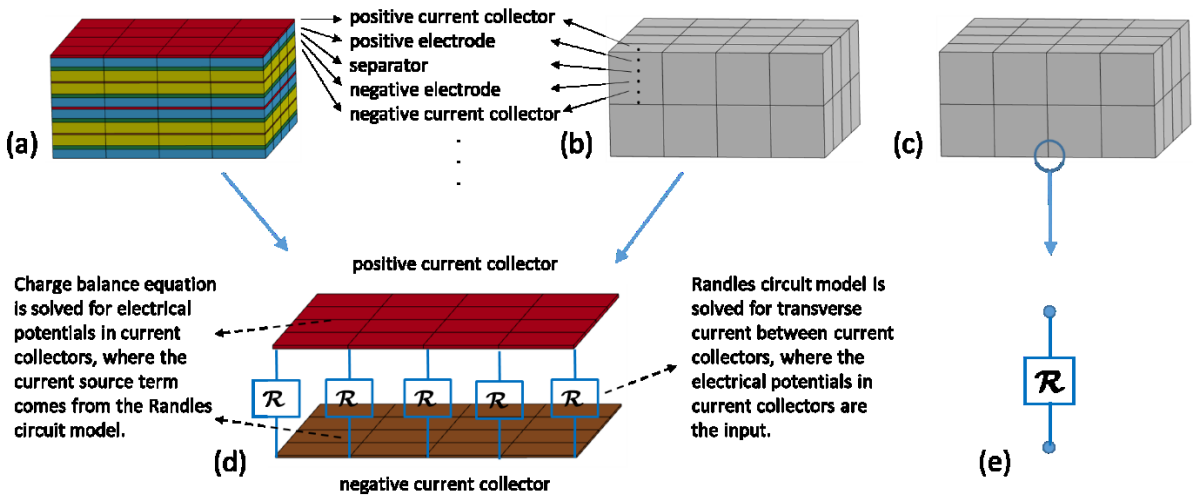

Figure 2: Comparison of (a, b, c) mesh and (d, e) Randles circuits used in the (a, d) solid model, (b, d) tshell model and (c, e) macro model. In (a), each individual component is resolved and represented by one layer of solid elements. The composite tshell elements in (b) and solid elements in (c) are much thicker than the elements in (a). One tshell element contains multiple integration points (black dots in (b)), and each of them represents one individual component. The network of Randles circuits in solid and tshell models is the same, where each Randle circuit connects a pair of nodes in neighboring current collectors (see (d)). In contrast, the macro model utilizes the homogenized material properties, and each node contains two independent electrical potentials connected by one Randles circuit (see (e)).

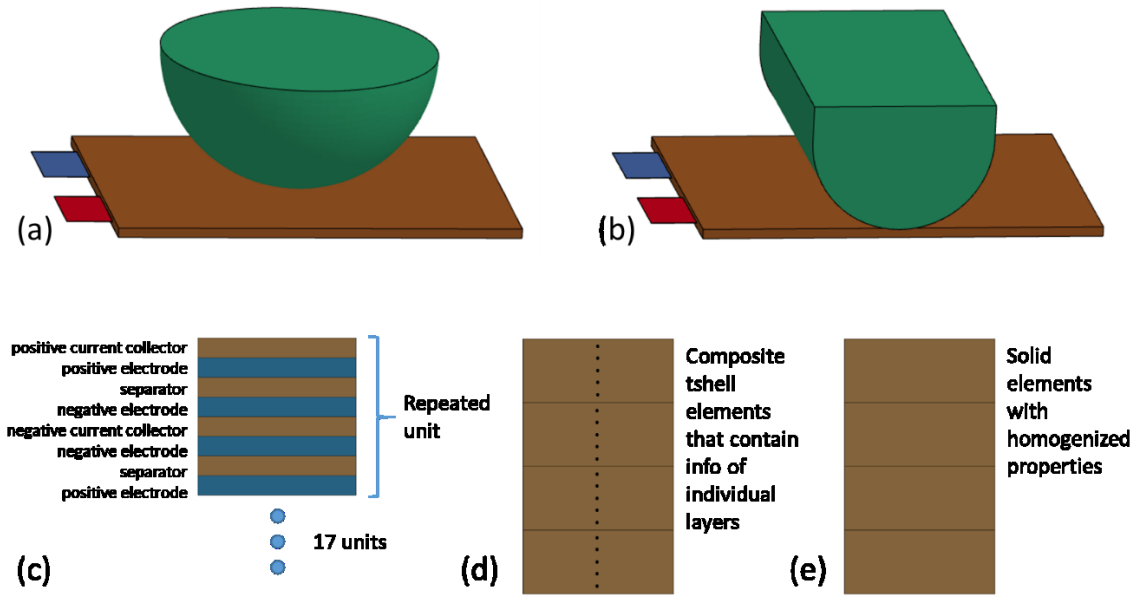

Figure 3: A pouch cell is impacted by an (a) semi-sphere and (b) semi-cylinder. Local cross-section view of a cell in the (c) solid, (d) tshell and (c) macro model.

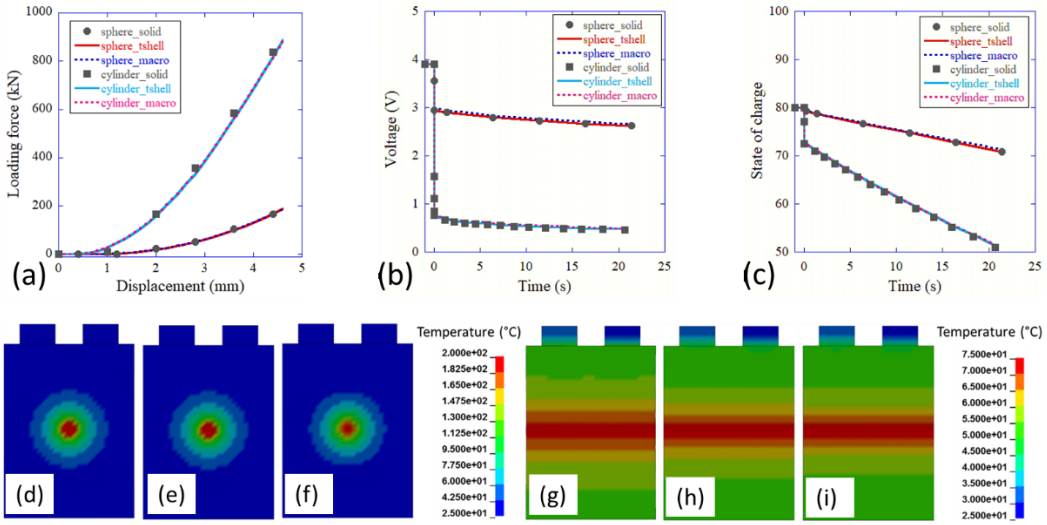

Figure 4: The evolution of (a) loading force, (b) voltage and (c) average SOC in different models. Comparison of temperature distribution at time 26s in (d, g) solid model, (e, h) tshell model and (f, i) macro model when a cell is impacted by a (d, e, f) semi-sphere and (g, h, i) semi-cylinder indenter.

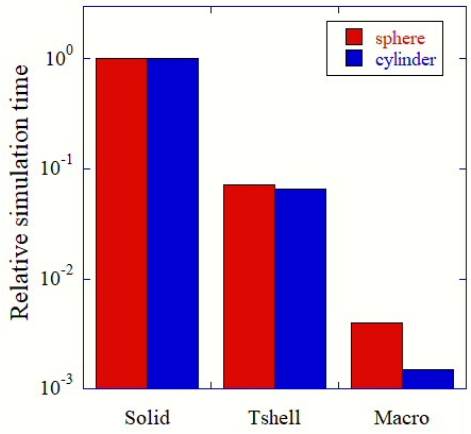

Figure 5: Relative simulation time in different models.

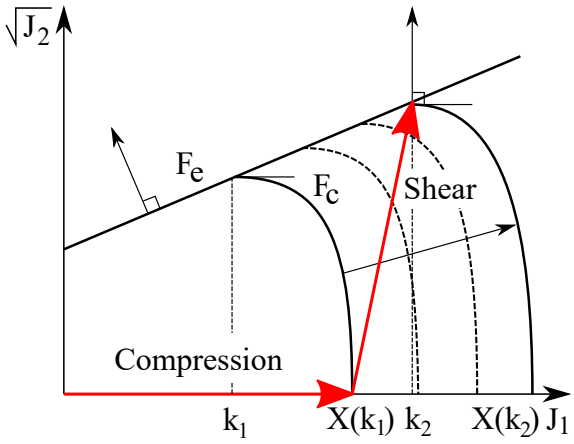

Figure 6: Triaxial Compression Test in Cap Model

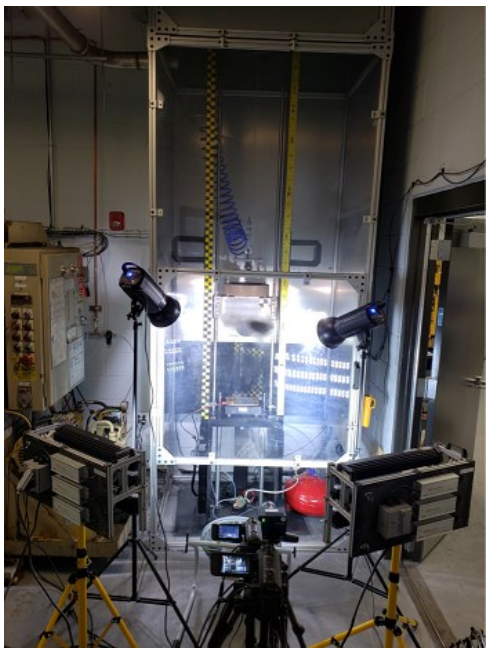

Figure 7: Fabricated impact stand with high-speed and conventional cameras set up.

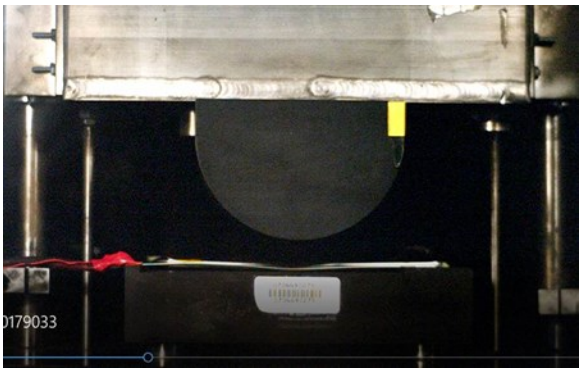

Figure 8: Still image of a high-speed video from impact testing, where a pouch cell is impacted by a semi-cylinder indenter.

Figure 9: Machined aluminum and anodized indenters and platens.

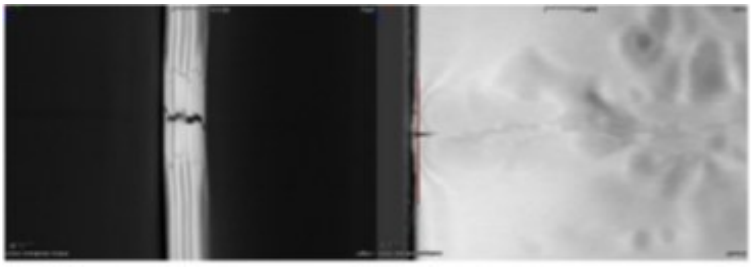

Figure 10: CT scan of a pouch cell impacted by a semi-cylinder indenter, where cracks are found at the edge of the cell center.

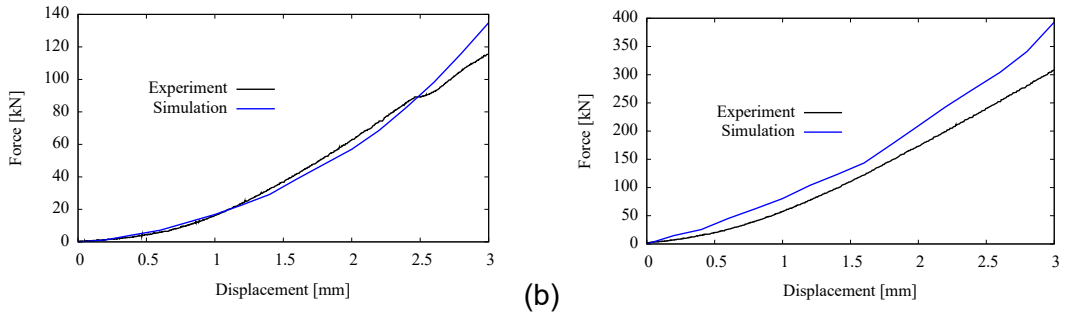

Figure 11: Comparison of experiments and simulations for quasi-static indentation experiments for (a) spherical and (b) cylindrical indenters.

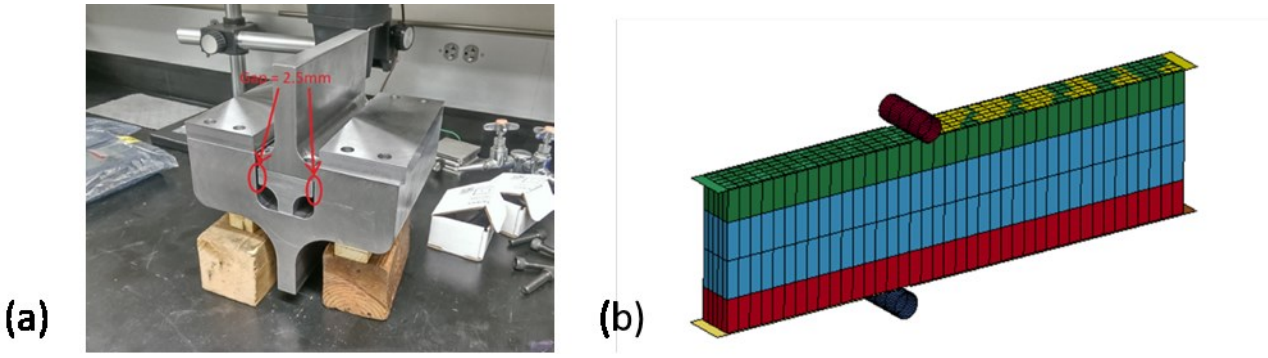

Figure 12: Shear test. (a) experimental setup, and (b) simulation model

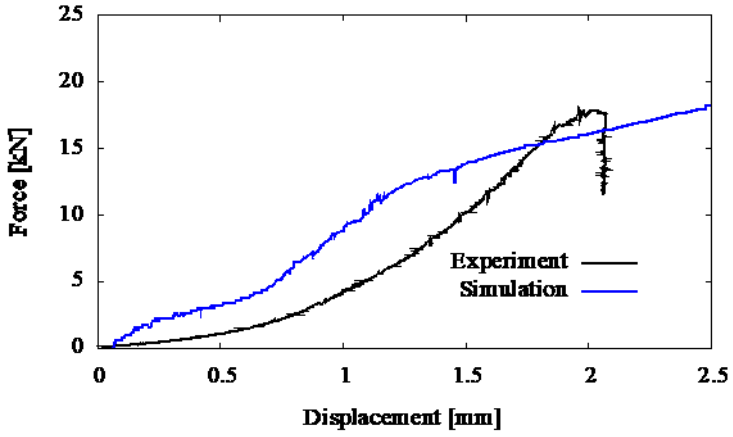

Figure 13: Comparison of experiment and simulation for quasi-static shear test

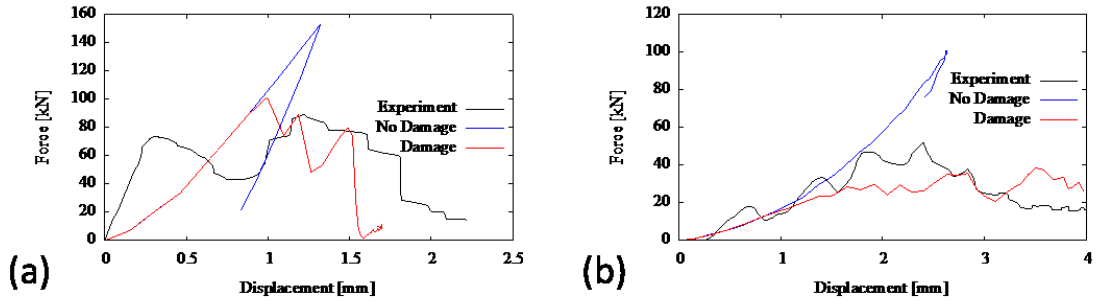

Figure 14: Comparison experimental and simulated forces for (a) cylindrical and (b) spherical impact.

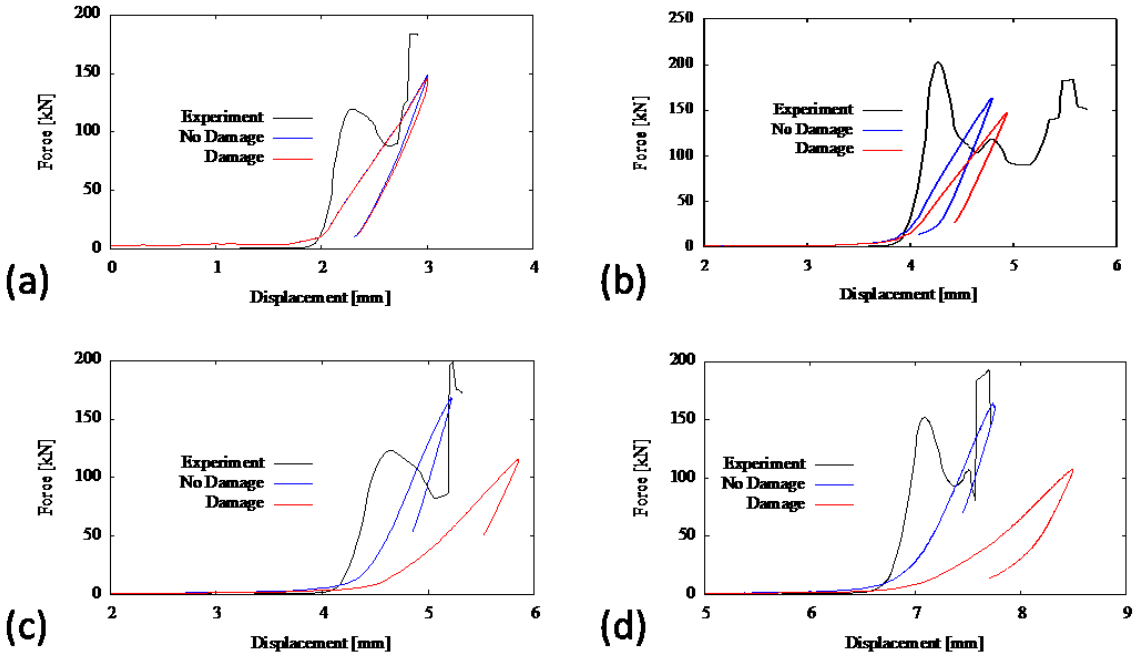

Figure 15: Comparison of experiments and simulations for groove depths: (a) 41%, (b) 100%, (c) 170% and (d) 200%.

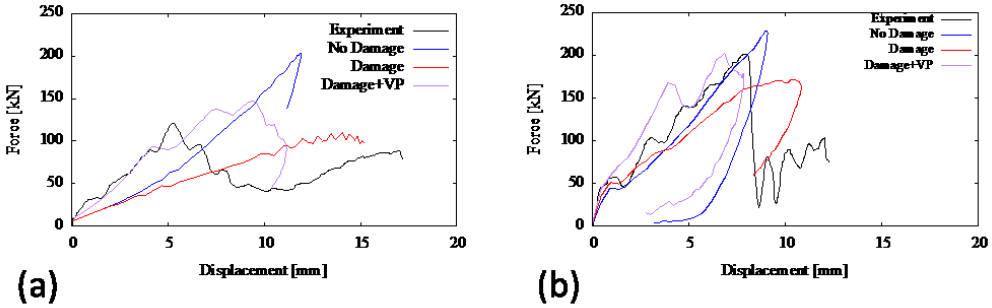

Figure 16: Comparison of simulation and experiments for Type-E cell impact with (a) spherical, and (b) cylindrical indenter.

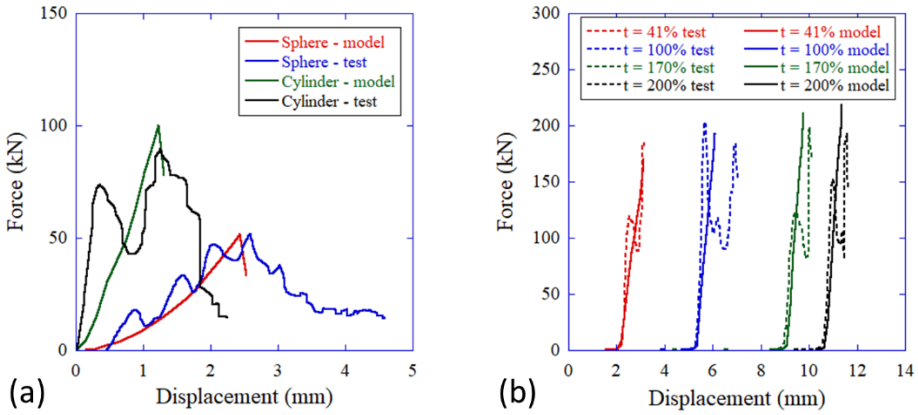

Figure 17: Compare model prediction and experimental measurement of force – displacement relationship when (a) a type D cell on a flat platen is impacted by a sphere or cylinder indenter; (b) a type D cell on platens with trough (trough depth ranges from 41% to 200% cell thickness) is impacted by a cylinder indenter. The cell SOC in all cases is 100%.

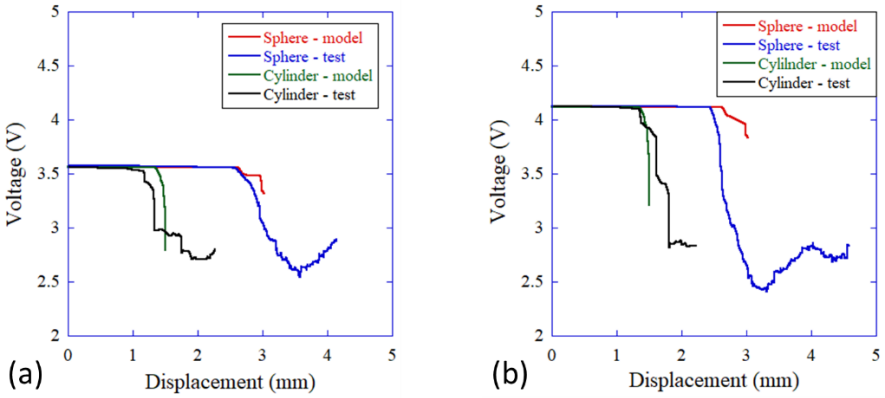

Figure 18: Compare model prediction and experimental measurement of voltage – displacement relationship when a type D cell with (a) 20% SOC and (b) 100% SOC on a flat platen is impacted by a sphere or cylinder indenter.

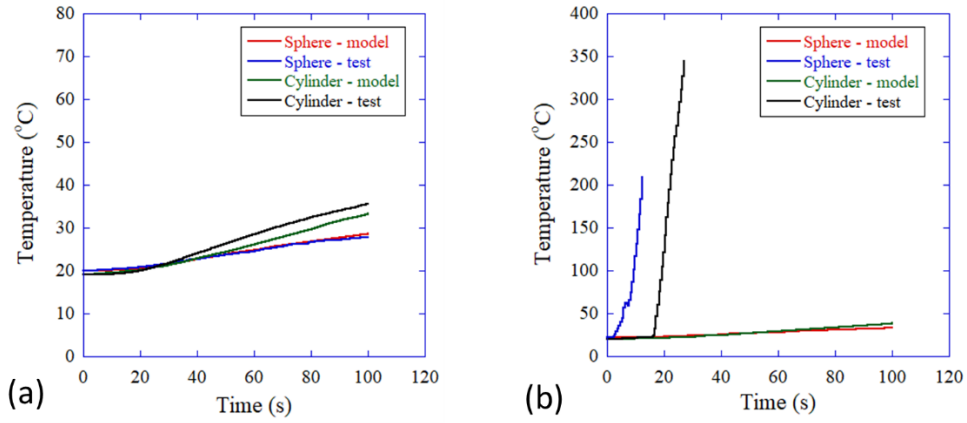

Figure 19: Compare model prediction and experimental measurement of temperature evaluation when a type D cell with (a) 20% SOC and (b) 100% SOC on a flat platen is impacted by a sphere or cylinder indenter.

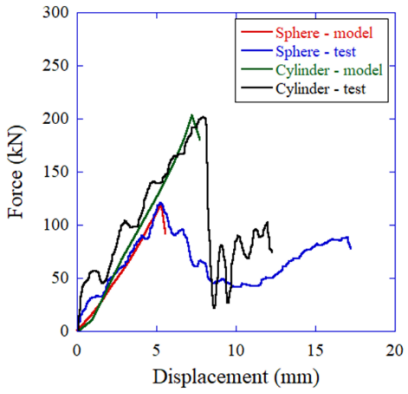

Figure 20: Compare model prediction and experimental measurement of force – displacement relationship when a type E cell is impacted by a sphere or cylinder indenter.

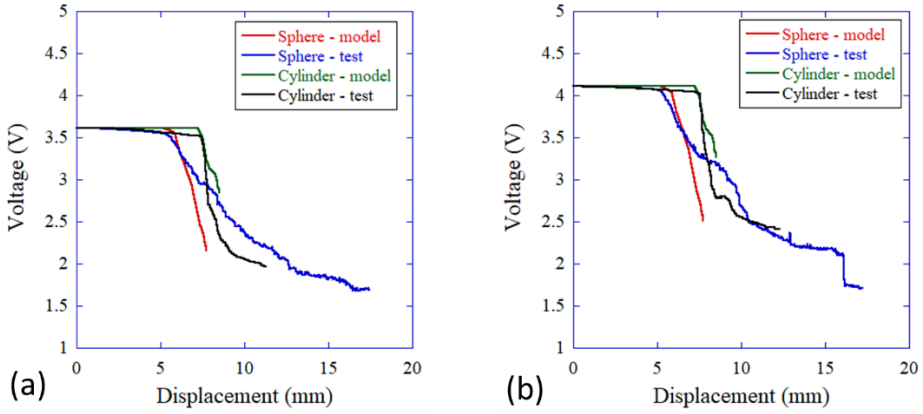

Figure 21: Compare model prediction and experimental measurement of voltage – displacement relationship when a type E cell with (a) 20% SOC and (b) 100% SOC is impacted by a sphere or cylinder indenter.

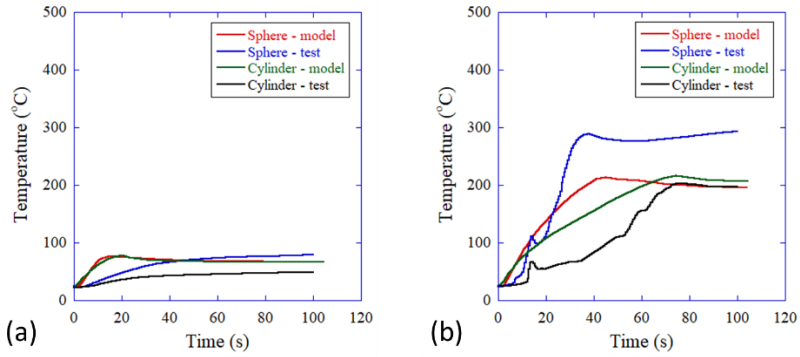

Figure 22: Compare model prediction and experimental measurement of temperature evaluation when a type E cell with (a) 20% SOC and (b) 100% SOC is impacted by a sphere or cylinder indenter.

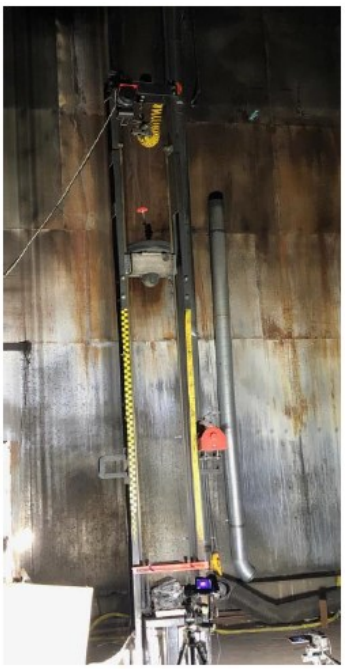

Figure 23: Module impact test stand.

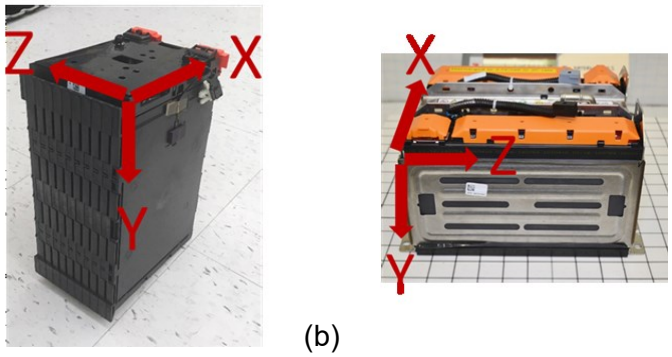

Figure 24: Impact orientations for (a) pouch modules and (b) prismatic modules.

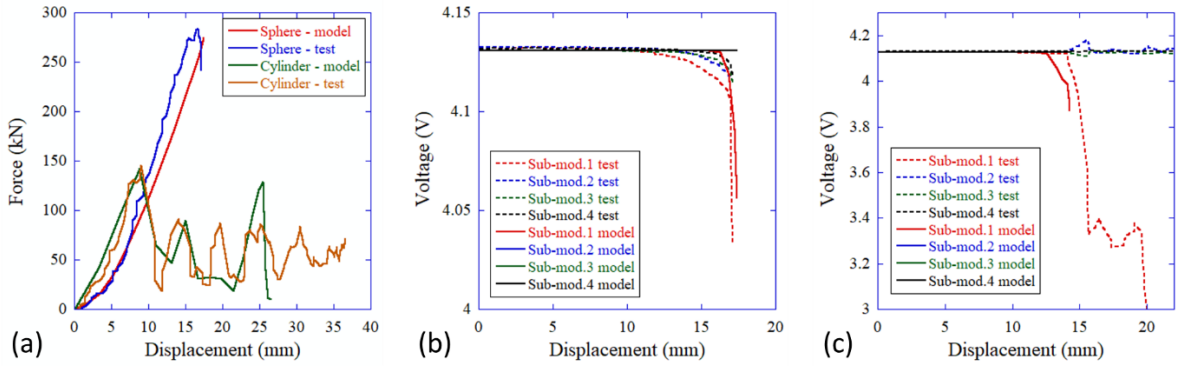

Figure 25: Compare model prediction and experimental measurement of (a) force – displacement relationship and (b, c) voltage-displacement relationship when a type D module is impacted by (a, b) a sphere or (a, c) a cylinder indenter along the Z direction.

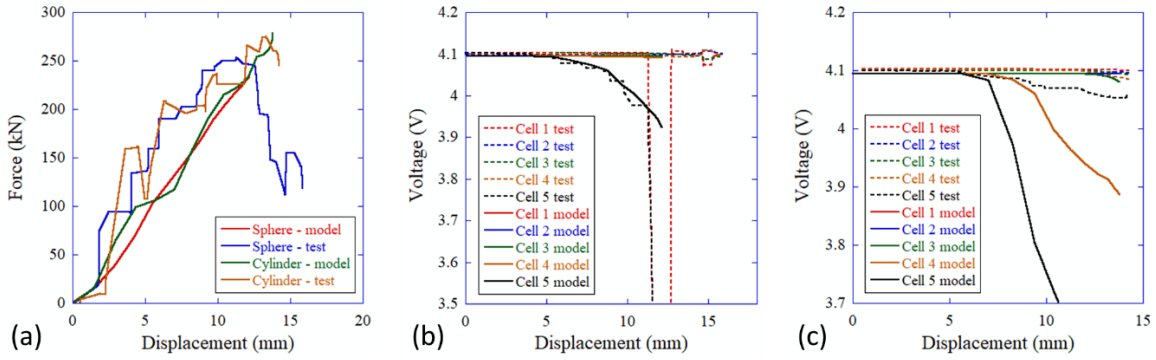

Figure 26: Compare model prediction and experimental measurement of (a) force – displacement relationship and (b, c) voltage-displacement relationship when a type E module is impacted by (a, b) a sphere or (a, c) a cylinder indenter along the Z direction.

8. Remarks:

9. Cost Status:

A Budget Status - Prime Recipient

- Ford spending throughout the project was on line and below budget. A balance of $154,014.00 remains from the original $3,625,000 ($154,014.00 remains from the original $4,375,000 budgeted for the total project). Table 7 shows the status through the end of the quarter.

B Budget Status – FFRDC/GOGO

- ORNL spending also was at all times within budget. A total of $750,000 has been spent, leaving a balance of $0 remaining from the original $750,000, see Table 8.

C FOLLOW-ON FUNDING

- Funding is limited to proposed project funding and cost-share as discussed during final negotiations. No follow-on funding is expected (however, a no-cost extension was granted to complete all tasks in 2020).

Table 7. Ford spending by quarter.

Spending Status for Battery Modeling Project DE-EE0007288								
Quarter	From	To	Estimated Federal Share of Outlays	Actual Federal Share of Outlays	Estimated Recipient Share of Outlays	Actual Recipient Share of Outlays	Cumulative Estimated	Cumulative Actual
BP1:	1/1/16 - 12/31/16							
4Q15	10/1/2015	12/31/2015		7,926		2,642		10,568
1Q16	1/1/2016	3/31/2016	137,582	124,639	50,021	41,546	187,603	176,752
2Q16	4/1/2016	6/30/2016	137,582	256,350	50,021	85,450	375,206	518,553
3Q16	7/1/2016	9/30/2016	137,582	67,898	50,021	22,633	562,808	609,084
4Q16	10/1/2016	12/31/2016	137,582	56,690	50,021	18,897	750,411	684,671
BP2:	1/1/17 - 12/31/17							
1Q17	1/1/2017	3/31/2017	234,655	91,223	74,289	30,408	1,059,355	806,301
2Q17	4/1/2017	6/30/2017	234,655	92,752	74,289	30,917	1,368,298	929,970
3Q17	7/1/2017	9/30/2017	234,655	79,334	74,289	26,445	1,677,242	1,035,749
4Q17	10/1/2017	12/31/2017	234,655	283,302	74,289	94,434	1,986,185	1,413,484
BP3:	1/1/18 - 12/31/18							
1Q18	1/1/2018	3/31/2018	315,263	93,694	94,441	31,231	2,395,889	1,538,409
2Q18	4/1/2018	6/30/2018	315,263	104,396	94,441	34,799	2,805,593	1,677,604
3Q18	7/1/2018	9/30/2018	315,263	198,627	94,441	66,209	3,215,296	1,942,441
4Q18	10/1/2018	12/31/2018	315,263	306,340	94,441	102,113	3,625,000	2,350,893
BP4:	1/1/19 - 12/31/19							
1Q19	1/1/2019	3/31/2019		71,684		23,895	3,625,000	2,446,471
2Q19	4/1/2019	6/30/2019		60,748		20,249	3,625,000	2,527,469
3Q19	7/1/2019	9/30/2019		434,857		144,952	3,625,000	3,107,279
4Q19	10/1/2019	12/31/2019		253,808		84,603	3,625,000	3,445,689
1Q20	1/1/2020	3/31/2020		18,973		6,324	3,625,000	3,470,986
	Program Total		**2,750,000**	**2,603,240**	**875,000**	**867,747**	**3,625,000**	**3,470,986**

Table 8. ORNL spending by quarter.

ORNL Spending Status						
Quarter	From	To	Estimated ORNL Spending	Actual ORNL Spending	Cumulative Estimated	Cumulative Actual
BP1:	1/1/2016 - 12/31/2016					
1Q16	1/1/2016	3/31/2016	62,500	30,340	62,500	30,340
2Q16	4/1/2016	6/30/2016	62,500	73,043	125,000	103,383
3Q16	7/1/2016	9/30/2016	62,500	34,430	187,500	137,813
4Q16	10/1/2016	12/31/2016	62,500	43,146	250,000	180,959
BP2:	1/1/2017 - 12/31/2017					
1Q17	1/1/2017	3/31/2017	62,500	28,920	312,500	209,879
2Q17	4/1/2017	6/30/2017	62,500	24,962	375,000	234,841
3Q17	7/1/2017	9/30/2017	62,500	39,236	437,500	274,077
4Q17	10/1/2017	12/31/2017	62,500	35,133	500,000	309,210
BP3:	1/1/2018 - 12/31/2018					
1Q18	1/1/2018	3/31/2018	62,500	43,078	562,500	352,289
2Q18	4/1/2018	6/30/2018	62,500	42,154	625,000	394,442
3Q18	7/1/2018	9/30/2018	62,500	38,089	687,500	432,532
4Q18	10/1/2018	12/31/2018	62,500	25,910	750,000	458,442
BP4:	1/1/2019 - 12/31/2019					
1Q19	1/1/2019	3/31/2019		23,792	750,000	482,234
2Q19	4/1/2019	6/30/2019		30,643	750,000	512,877
3Q19	7/1/2019	9/30/2019		25,971	750,000	538,848
4Q19	10/1/2019	12/31/2019		126,209	750,000	665,057
1Q20	1/1/2020	3/31/2020		84,943	750,000	750,000
	Program Total		**750,000**	**750,000**	**750,000**	**750,000**

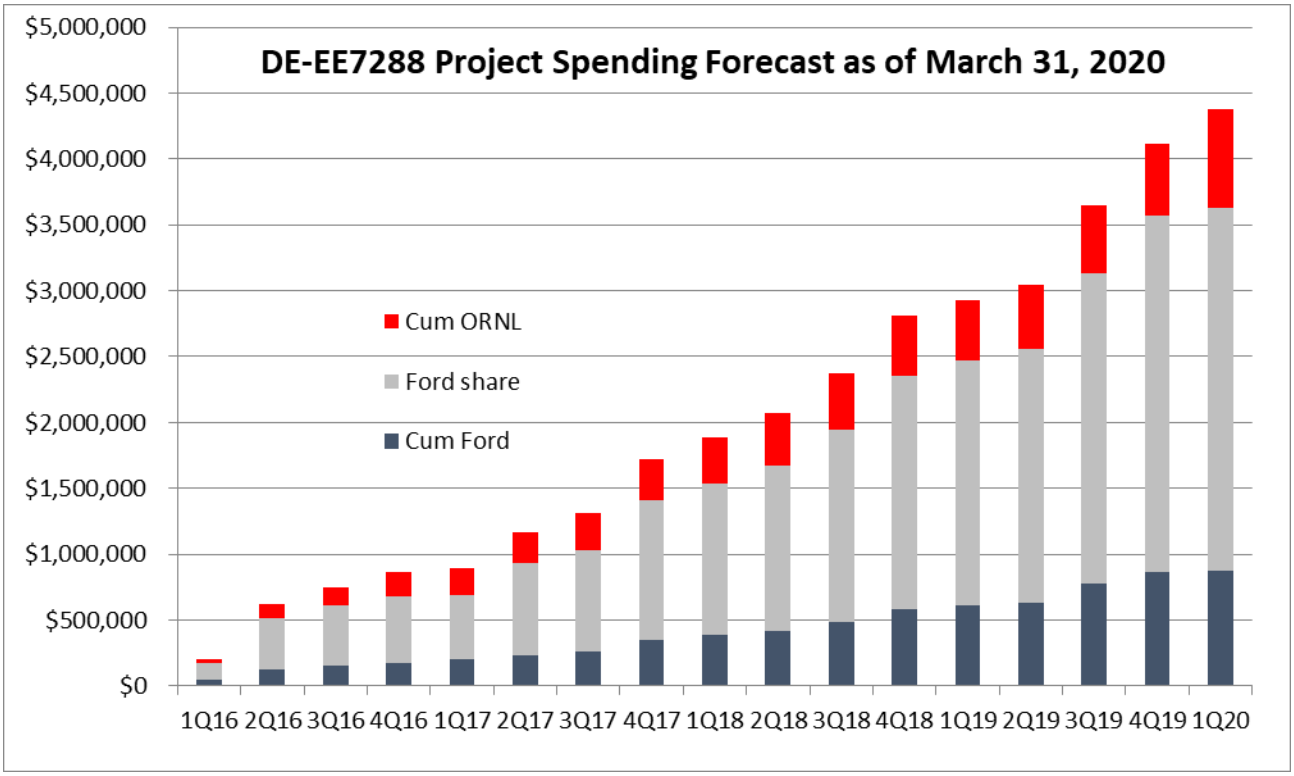

Figure 26. Total spending through end of project.

10. Patents / Patent Applications:

11. Publications/Presentations:

- Publications:

1. J. Marcicki, A. Bartlett, X. Yang, V. Mejia, M. Zhu, Y. Chen, P. L'Eplattenier, I. Caldichoury, Battery abuse case study analysis using LS-DYNA, LS-DYNA conference proceedings, 2016.
2. P. L'Eplattenier, I. Caldichoury, J. Marcicki, A. Bartlett, X. Yang, V. Mejia, M. Zhu, Y. Chen, A distributed Randle circuit model for battery abuse simulations using LS-DYNA, LS-DYNA conference proceedings, 2016.
3. J. Marcicki, M. Zhu, A. Bartlett, X. Yang, Y. Chen, T. Miller, P. L'Eplattenier, I. Caldichoury, A simulation framework for battery cell impact safety modeling using LS-DYNA, J. Electrochem. Soc., 164, A6440-A6448, 2017.
4. H. Xu, M. Zhu, J. Marcicki, X. Yang, Mechanical modeling of battery separator based on microstructure image analysis and stochastic characterization, J. Power Sources, 345, 137-145, 2017.
5. J. Deng, C. Bae, J. Marcicki, A. Masias, T. Miller, Safety modelling and testing of lithium-ion batteries in electrified vehicles. Nature Energy. 3, 261-266, 2018.
6. J. Deng, C. Bae, T. Miller, P. L'Eplattenier, S. Bateau-Meyer, Accelerate battery safety simulations using composite tshell elements. J. Electrochem. Soc. 165, A3067-A3076, 2018.
7. J. Deng, M. Zhu, C. Bae, T. Miller, P. L'Eplattenier, S. Bateau-Meyer, Safety modeling of lithium-ion batteries under mechanical abuse, LS-DYNA conference proceedings, 2018.
8. S. Bateau-Meyer, P. L'Eplattenier, J. Deng, M. Zhu, C. Bae, T. Miller, Randles circuit parameters set up for battery simulations in LS-DYNA, LS-DYNA conference proceedings, 2018.
9. J. Deng, C. Bae, T. Miller, P. L'Eplattenier, I. Caldichoury, Communication – Multi-physics battery safety simulations across length scales. J. Electrochem. Soc. 166, A3119-A3121, 2019.
10. H. Xu, C. Bae, Stochastic 3D microstructure reconstruction and mechanical modeling of anisotropic battery separators, J. Power Sources, 430, 67-73, 2019
11. J. Deng, C. Bae, A. Denlinger, T. Miller, Electric vehicles batteries: requirements and challenges, Joule, 4, 511-515, 2020.
12. J. Deng, C. Bae, T. Miller, M. Zhu, P. L'Eplattenier, I. Caldichoury, Lithium-ion battery multi-physics simulations using LS-DYNA, LS-DYNA conference proceedings, 2020.
13. S. Simunovic, L. Binderman, A. Kumar, Modeling of deformation of battery cells using thick shell element formulation, Comput. Methods Appl. Mech. Engre. 362, 112840, 2020
14. J. Deng, I. Smith, C. Bae, P. Rarigh, T. Miller, B. Surampudi, P. L'Eplattenier, I. Caldichoury, Impact modeling and testing of pouch and prismatic cells, J. Electrochem. Soc.
15. J. Deng, S. Simunovic, A. Kumar, I. Smith, P. Rarigh, M. Zhu, C. Bae, T. Miller, B. Surampudi, Mechanical modeling and testing of pouch cells under various loading conditions, in preparation.

- Conference presentations:

1. J. Marcicki, A. Bartlett, X. G. Yang, V. Mejia, M. Zhu, Y. Chen, P. L'Eplattenier, and I. Caldichoury, A Simulation Framework for Battery Safety Modeling, 229th ECS Meeting, San Diego, CA, May 29 - Jun. 2, 2016.
2. J. Marcicki, A. Bartlett, X. Yang, V. Mejia, M. Zhu, Y. Chen, P. L'Eplattenier, I. Caldichoury, Battery abuse case study analysis using LS-DYNA, 14th LS-DYNA International Conference, Dearborn, MI, Jun. 12-14, 2016.
3. P. L'Eplattenier, I. Caldichoury, J. Marcicki, A. Bartlett, X. Yang, V. Mejia, M. Zhu, Y. Chen, A distributed Randle circuit model for battery abuse simulations using LS-DYNA, 14th LS-DYNA International Conference, Dearborn, MI, Jun. 12-14, 2016.
4. J. Marcicki, A. Bartlett, X. G. Yang, V. Mejia, M. Zhu, Y. Chen, P. L'Eplattenier, and I. Caldichoury, A Simulation Framework for Battery Safety Modeling, 16th Annual Advanced Automotive Battery Conference, Detroit, MI, Jun. 14-17, 2016
5. J. Deng, M. Zhu, C. Bae, T. Miller, P. L'Eplattenier, Multi-physics modeling of impact safety of lithium-ion batteries, 232nd ECS Meeting, National Harbor, MD, Oct. 1-6, 2017.
6. J. Deng, M. Zhu, C. Bae, T. Miller, P. L'Eplattenier, Multi-physics modeling of impact safety of lithium-ion batteries, 4th Ford Global Control Conference, Dearborn, MI, Dec. 6-7, 2017.
7. J. Deng, M. Zhu, C. Bae, T. Miller, P. L'Eplattenier, S. Bateau-Meyer, Safety modeling of lithium-ion batteries under mechanical abuse, 15th LS-DYNA International Conference, Dearborn, MI, Jun. 11-12, 2018.
8. S. Bateau-Meyer, P. L'Eplattenier, J. Deng, M. Zhu, C. Bae, T. Miller, Randles circuit parameters set up for battery simulations in LS-DYNA, 15th LS-DYNA International Conference, Dearborn, MI, Jun. 11-12, 2018.
9. J. Deng, M. Zhu, C. Bae, T. Miller, P. L'Eplattenier, Modeling impact safety of lithium-ion batteries in electrified vehicles, 236th ECS Meeting, Atlanta, GA, Oct. 13-17, 2019.
10. J. Deng, C. Bae, T. Miller, Min. Zhu, P. L'Eplattenier, I. Caldichoury, Lithium-ion battery safety simulations using LS-DYNA, 16th LS-DYNA International Conference, Detroit, MI, May 31-Jun. 2, 2020.

Appendix

Mesh	Type	Cathode Chemistry and Format	Cell	Module	Pack
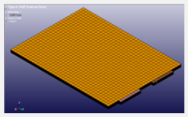	A	NMC//LMO Blend Pouch	15 Ah 3.7 V 0.06 kWh	4P1S 5P4S	4S5P (x9) + 2S5P (x2)
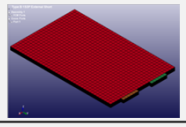	B	NMC Pouch	20 Ah 3.6 V 0.07 kWh	3P1S and 3P10S	
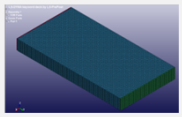	C	LFP Prismatic	18 Ah 3.2 V 0.06 kWh	4P1S 5P2S	36S5P
TBD	D	**NMC Pouch**	**21 Ah 3.65 V**	**5P4S**	**4S5P (x9) + 2S5P (x2)**
TBD	E	**Metal Oxide Blend Prismatic**	**60 Ah 3.65 V (est)**	TBD	

Legacy Hardware ☐ **Hardware sourced for this project** ☐

Figure 27. List of cells being studied. Cells A-C were used for testing in previous projects; cells D and E have been purchased to support additional validation testing in this project.